DOI: 10.15825/1995-1191-2025-3-125-133

# OPTIMIZATION OF IMPELLER DESIGN IN THE ROTAFLOW CENTRIFUGAL PUMP

A.P. Kuleshov, N.V. Grudinin, A.S. Buchnev

Shumakov National Medical Research Center of Transplantology and Artificial Organs, Moscow, Russian Federation

As part of the development of a domestic counterpart, the impeller of the RotaFlow centrifugal pump (Maquet, Germany) was modernized within the framework of research into the operating conditions of centrifugal pumps used in extracorporeal membrane oxygenation (ECMO) therapy. A novel rotor impeller design was proposed, featuring two types of blades: the primary elongated blades responsible for generating most of the pressure, and secondary shortened auxiliary blades. A three-dimensional computational model of the RotaFlow pump was created incorporating the redesigned impeller. To evaluate the effectiveness of the modernization, the new design was compared to the original Maquet impeller. Computational simulations were conducted to analyze key fluid dynamics parameters, such as turbulence intensity and flow velocity, within the typical operating range of the pump (flow rates from 1 to 5 L/min at a pressure drop of 350 mmHg). Mathematical modeling demonstrated that the new blade configuration yields improved flow characteristics compared to the original design.

Keywords: 3-dimensional computer model, centrifugal pump, turbulence, impeller.

#### INTRODUCTION

Although ECMO pumps are designed for specific flow rates and pressures, in practice they are frequently used across a wide range of hemodynamic conditions. In certain clinical scenarios, these pumps must generate high pressures of 300–400 mmHg to overcome the resistance of the oxygenator membrane and deliver flow rates of up to 5 L/min to meet the patient's needs [1].

Centrifugal pumps commonly used in ECMO are compact, with impeller diameters not exceeding 50 mm, such as the RotaFlow (Maquet, Germany) [2], CentriMag (USA) [3], and Deltastream Medos (Germany) [4]. However, reducing impeller size inevitably requires higher rotational speeds and results in larger incremental changes when adjusting hemodynamic parameters. Empirical data indicate that halving the impeller diameter reduces efficiency by 5–10 percentage points [5], largely due to altered surface area—to—volume ratios and increased hydraulic losses.

Small pumps are often operated in ECMO at minimal flow rates, even though they are designed for higher operating points. This mismatch reduces efficiency and increases turbulence and stagnant flow zones, as blood spends more time within the pump. Operating outside the intended range of application further decreases efficiency and, at higher speeds, prolongs blood exposure to shear stress, thereby exacerbating hemolysis [6].

Shear stress and increased blood exposure time dramatically elevate hemolysis, while the thrombogenic potential of ECMO circuits is also attributed to mechanical factors that trigger biochemical cascades. Hastings et al.

[7] investigated thrombus formation *in vivo*, showing that the centrifugal pump, tubing, and connectors are the main contributors to thrombogenesis within ECMO systems.

Today, evaluation methods allow for pump performance testing not only under validated conditions for left ventricular bypass (LVB) [8–10], but also under ECMO-specific conditions [11]. Importantly, pumps optimized for favorable flow characteristics in LVB may not demonstrate comparable performance in ECMO, underscoring the limitations of their universal application.

The most appropriate solution would be the development of a range of pumps tailored to specific applications, with effective flow and pressure ranges designed for different clinical modes and compatible with oxygenators of varying resistance. An example of this approach is the Jarvik family of implantable systems [12]. However, such specialization is prohibitively expensive, and in practice, pumps continue to be used as universal components across all ECMO operating modes.

A more feasible alternative is to optimize or redesign the pump impeller. The goal of such improvements is either to reduce rotational speed while maintaining the required pressure and flow, or to enhance fluid dynamics within the pump, thereby shortening blood exposure time. In this study, we propose a method for optimizing the RotaFlow pump impeller. The modification reduces hemolysis by lowering the impeller's rotational speed and improves overall pump performance under highload conditions.

Corresponding author: Arkady Kuleshov. Address: 1, Shchukinskaya str., Moscow, 123182, Russian Federation.

#### MATERIALS AND METHODS

The following section provides an overview of the process used to upgrade the rotor of a RotaFlow pump. The initial stage involved scanning the pump components to reconstruct a detailed 3D model. Scanning was performed using a 3DMakerpro Seal 3D scanner (China), achieving an accuracy of 0.01 mm. Based on the scanned images, sketches and 3D designs of each component were created individually. The final pump assembly was rendered in the SolidWorks PhotoView 360 graphics module, where materials and textures were applied. The resulting model of the pump is shown in Fig. 1.

The pump rotor is divided into two elements: cap and impeller. The impeller, in turn, consists of blades specifically designed to generate pressure while minimizing shear stress on the blood flowing through the pump. This model consists of a combination of two types of blades: a primary elongated blade and an secondary shortened blade. This configuration aims to reduce hemolysis by improving flow distribution and lowering localized shear stresses. An example of the conversion from the original impeller design to the optimized configuration is shown in Fig. 2.

The blade combination incorporates an equal number of each blade type – three primary elongated blades and three secondary shortened blades – arranged alternately on the cap to ensure sectoral symmetry. Each primary blade is positioned 50° behind the subsequent secondary blade in a clockwise direction. The secondary blade is a truncated version of the primary blade, with its length reduced to one-third of the primary blade.

Both blade types feature a streamlined profile, constructed using a simplified geometric method in which the blades are defined along a circular arc. This profile was further optimized through computational hydrodynamic modeling to minimize shear stress on the blood as it passes through the device.

The process of creating the impeller is illustrated in Fig. 3, which presents a schematic drawing of the blade construction and the profile of the central arc.

The blade construction proceeds as follows. Circles 1 and 2 are drawn at the beginning and end of the blade, with diameters  $D_1$  and  $D_2$ , respectively. On the end circle (2), point A is selected and connected to the circle center O. From radius OA, an angle equal to the sum of the inlet ( $\beta_1$ ) and outlet ( $\beta_2$ ) blade angles is measured. At this angle, draw radius OB on the starting circle (1). The intersection of segment OB with circle (1) defines point C. A ray is then drawn through points A and C until it intersects the wheel inlet circle at point D. Point D represents the starting point of the blade, while point A is its endpoint. From A, a ray is drawn at an angle  $\beta_2$  relative to AO, measured counterclockwise. From the midpoint E of segment AD, a perpendicular is dropped, intersecting the ray from A at point  $O_1$ . Point  $O_1$  becomes

the arc center, with segments  $AO_1$  and  $EO_1$  equal to the blade arc radius  $R_L$ . With  $O_1$  as the center, arc AD is drawn, forming the centerline of the blade profile. Conventionally, arc AD is taken as the blade length. Under



Fig. 1. Reconstructed 3D model of the RotaFlow pump (Maquet, Germany)

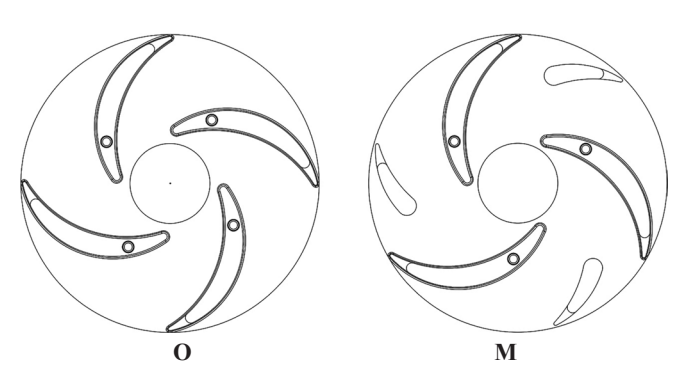


Fig. 2. Impeller blade profiles of the original (O) and modified (M) RotaFlow pump designs

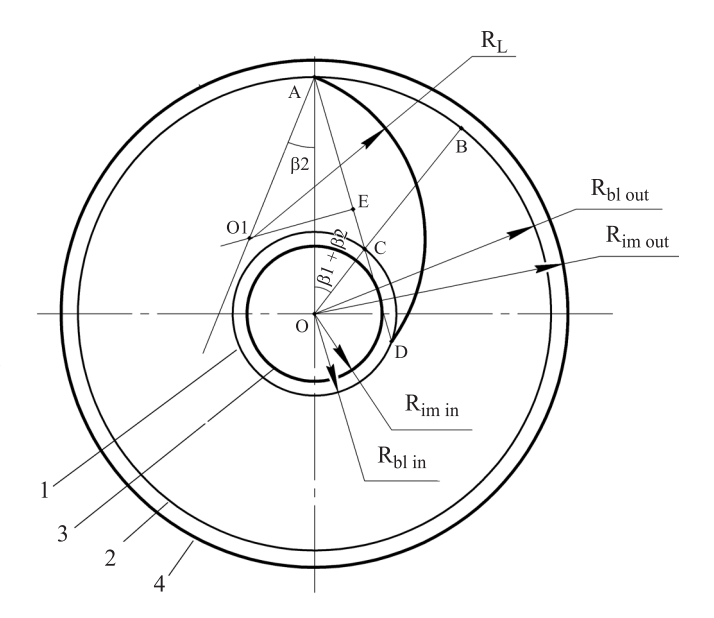


Fig. 3. Structural design of the main blade in the modified RotaFlow pump impeller. Abbreviations:  $R_{bl \ in}$ , inlet blade radius;  $R_{im \ in}$ , inlet impeller radius;  $R_{bl \ out}$ , outlet blade radius;  $R_{im \ out}$ , outlet impeller radius

boundary conditions, the blade tip circle and blade root circle coincide with the rotor inlet diameter (3) and the rotor diameter (4). In this case, the radius of the wheel blades is determined by formula (1):

$$R_{L} = \frac{\left(\frac{D_{2}}{2}\right)^{2} - \left(\frac{D_{1}}{2}\right)^{2}}{D_{2} \cdot \cos \beta_{2} - D_{1} \cdot \cos \beta_{2}}.$$
 (1)

The profiles of the inner and outer walls of the main blade were constructed using the same geometric method, with parameter adjustments applied to define the blade thickness (Fig. 3, b). In the example shown, the middle arc of the blade was designed with an inlet angle ( $\beta_1$ ) of 33° and an outlet angle ( $\beta_2$ ) of 22° for the modified model. In practice, the inlet and outlet angles can vary between 10° and 60°, depending on hydrodynamic calculations tailored to the specific operating conditions of the device.

The additional blade was constructed using the same method as the main blade, but with the arc length reduced to one-third of the main blade's arc. Among several design variations tested, the ½ length ratio provided the optimal performance, outperforming both shorter (¼) and longer (½) blade ratios.

Each blade includes a localized thickening at the midpoint of the curvature, with a maximum thickness of no more than 4 mm. This corresponds to approximately 1.5–2 times the thickness at the trailing edge.

# Computational fluid dynamics (CFD) analysis

The geometries of the two pumps, reconstructed from measurements of actual device components, were converted into CAD format for export to computer-aided design systems. Numerical simulations of flow inside the three pump configurations were performed using a commercial computational fluid dynamics (CFD) package FLUENT 14.2 (ANSYS Inc., Canonsburg, Pennsylvania). Both structured and unstructured meshes were employed to compute flow fields, with details of the meshing procedure available in [13].

Flow distribution was obtained by numerically solving the governing fluid dynamics equations using an unstructured finite-volume mesh in FLUENT 14.2. Zero-pressure and high-pressure boundary conditions were applied at the pump inlet and outlet, respectively, corresponding to the pressure head the pump is expected to overcome at a given rotational speed. Pump walls were assumed rigid, with a specified roughness of 5  $\mu$ m, representative of die-cast surface quality.

Blood was modeled as an incompressible Newtonian fluid, with a density of  $1060 \text{ kg/m}^3$  and a viscosity of  $0.003763 \text{ Pa} \cdot \text{s}$  [14]. The standard k- $\epsilon$  turbulence model was applied to solve the flow equations. Simulations were performed at pump rotation speeds of 2000, 2500, 3000, and 3500 rpm. Solution convergence was defined at  $10^{-4}$ .

For both the computational model and the physical mock-up, the rotor speed range was set between 1100 and 3500 rpm. In the numerical model, a minimum mesh element size of  $50 \, \mu m$  (tetrahedral elements) was applied. This resolution provided a balance between accuracy and computational efficiency, allowing simulations to be performed with less time and software resources.

# Modeling of flow and head-capacity curve (HCC) characteristics

The head-capacity curve of two impeller designs — the original and the modified — were evaluated using the frozen rotor method. At the pump inlet, the pressure was set to 1 mmHg, while the outlet pressure was adjusted to achieve flow rates ranging from 1 to 5 L/min. Minimum turbulence conditions were imposed at the inlet, with an intensity of 1% and a turbulence scale of 0.1 mm.

Simulation and analysis of flow in ECMO operating mode were carried out under slightly modified boundary conditions. In this case, pressure—flow characteristics were assessed for both pumps at an outlet pressure of 350 mmHg, with flow rates of 1, 3, and 5 L/min. To account for increased turbulence under these operating conditions, the inlet turbulence parameters were doubled, which now had the following values.

Under these conditions, the flow distribution and turbulence parameters (turbulence intensity and turbulence scale) were evaluated across different areas of the pump, including the horizontal section of the rotor. Analytical comparisons of turbulence patterns between the two impeller designs were then performed.

A numerical assessment of turbulence was conducted using the Reynolds number (Re). The highest flow velocities were observed at the outlet of the rotor channels, while lower velocities were detected at the pump inlet and outlet regions. The Reynolds number was calculated for the flow domain based on simulation data and using formula (2):

$$Re_{imp} = \frac{2r^2\omega}{\upsilon},$$

$$\upsilon = \eta/\rho,$$
(2)

where dynamic viscosity  $\eta = 0.0035 \text{ kg} \cdot \text{m}^{-1} \cdot \text{s}^{-1}$ ; blood density  $\rho = 1050 \text{ kg} \cdot \text{m}^{-3}$ ;  $\omega - \text{permissible maximum rotor}$  angular velocity; r - rotor radius.

## **RESULTS**

#### Hydrodynamic characteristics

The CFD models were evaluated by comparing the numerically predicted head of the original rotor design with that of the optimized design. The pressure–flow relationships are presented in Fig. 4.

In the graphs, solid lines correspond to the fourbladed rotor prior to modification, while dashed lines represent simulation data for the redesigned rotor with three long and three short blades. The line colors indicate the specified pump rotational speed. An increase in head is observed when the rotor is optimized.

### Turbulence and flow distribution

Fig. 5 illustrates fluid motion in the transverse axial section of the volute at the rotor outlet. The flow struc-

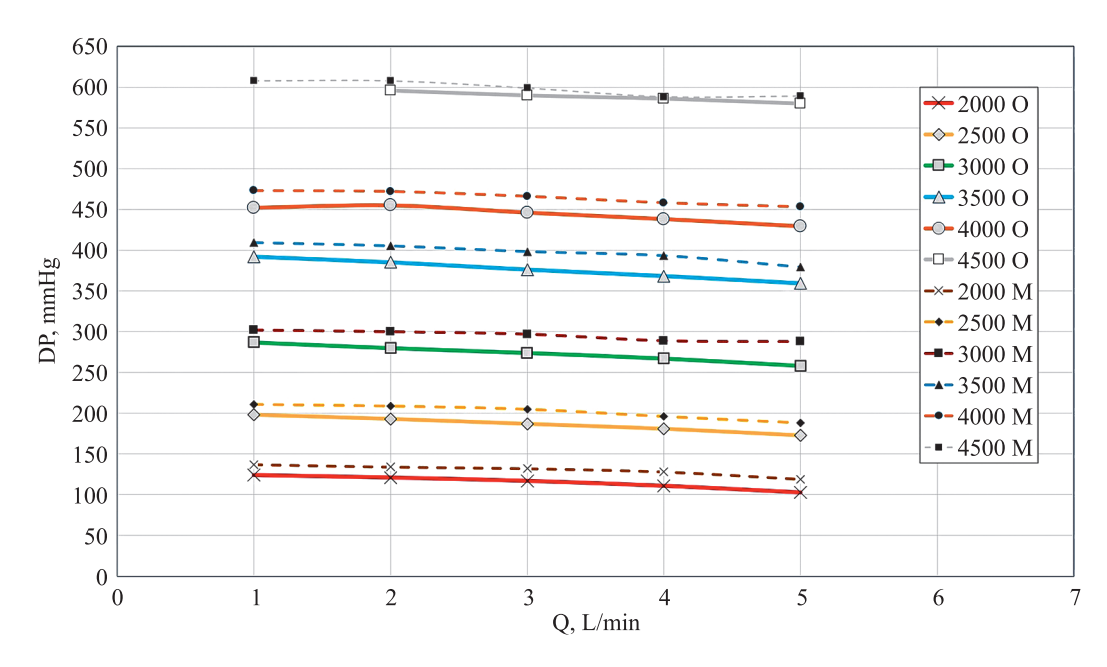


Fig. 4. Measurement of the Rotaflow pump's head-capacity curve (HCC). Solid lines represent the original rotor, dashed lines correspond to the modified rotor

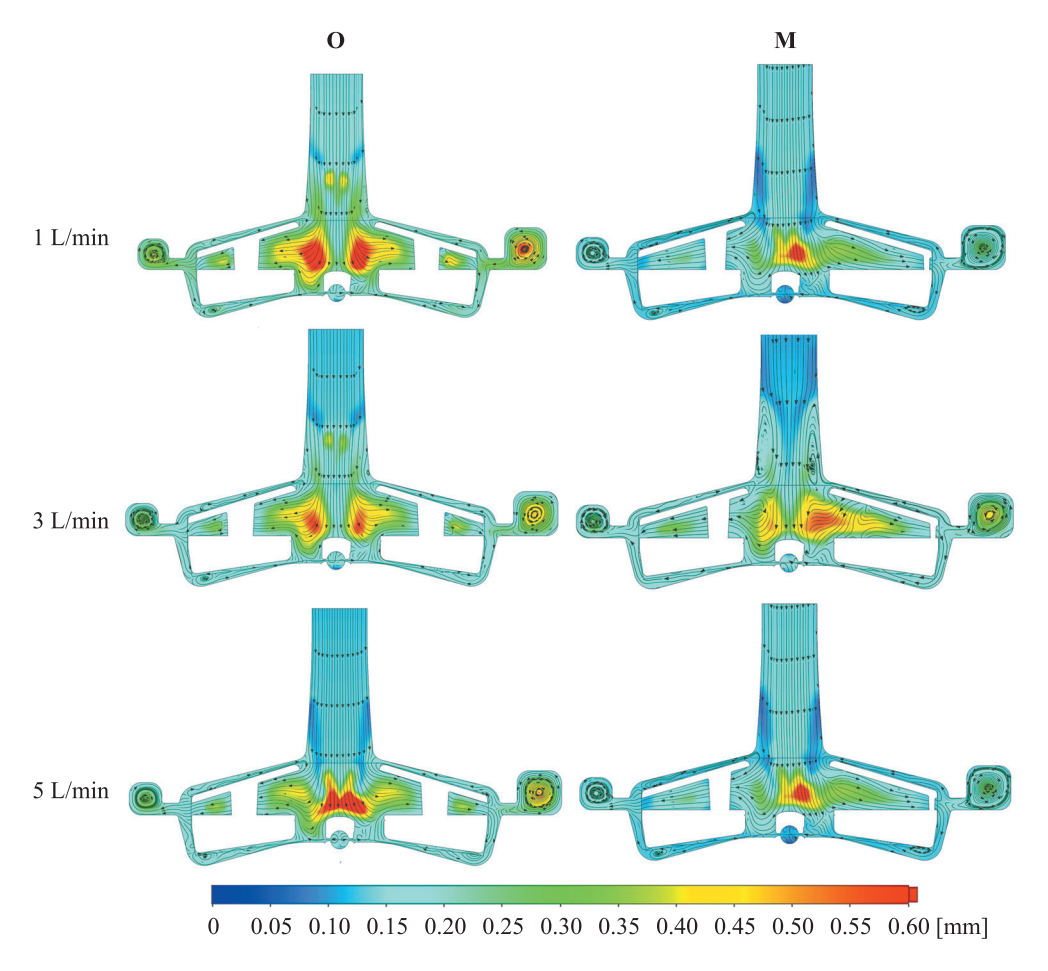


Fig. 5. Distribution of turbulence intensity in a cross-sectional view of the pump, comparing the original (O) and modified (M) impeller designs

ture in the section perpendicular to the radial stream exhibits a symmetrical vortex that fills the entire outlet area. The color scale indicates turbulence levels (scale and intensity) at flow rates of 1, 3, and 5 L/min. Velocity distributions in the longitudinal section are shown in Fig. 6.

Table 1 presents the numerical changes in flow structure, highlighting the dynamics of blood flow improvement achieved with the optimized impeller design. Key turbulent flow parameters – scale, intensity, and exposure time – were analyzed.

A numerical assessment of turbulence was also performed using the Reynolds number (Re). The highest flow velocities were observed at the outlet of the rotor channels, while significantly lower velocities were recorded at both the pump inlet and outlet regions.

#### DISCUSSION

The calculations and experimental tests of the two centrifugal pump samples demonstrated that hydrodynamic performance can be moderately improved without the need for a complete redesign of the pump. The head-capacity curve of the optimized rotor maintained flat flow characteristics up to 5 L/min, consistent with typical centrifugal pump behavior, while the average pressure at a fixed rotational speed increased by 80–90 mmHg.

This improvement allows the rotor speed to be reduced by 70–100 rpm, resulting in an increase in hydraulic efficiency of approximately 3–5%. In addition, the sixblade configuration enhanced flushing of the central axial zone, thereby reducing exposure time. The maximum particle passage time decreased by 0.10–0.15 seconds.

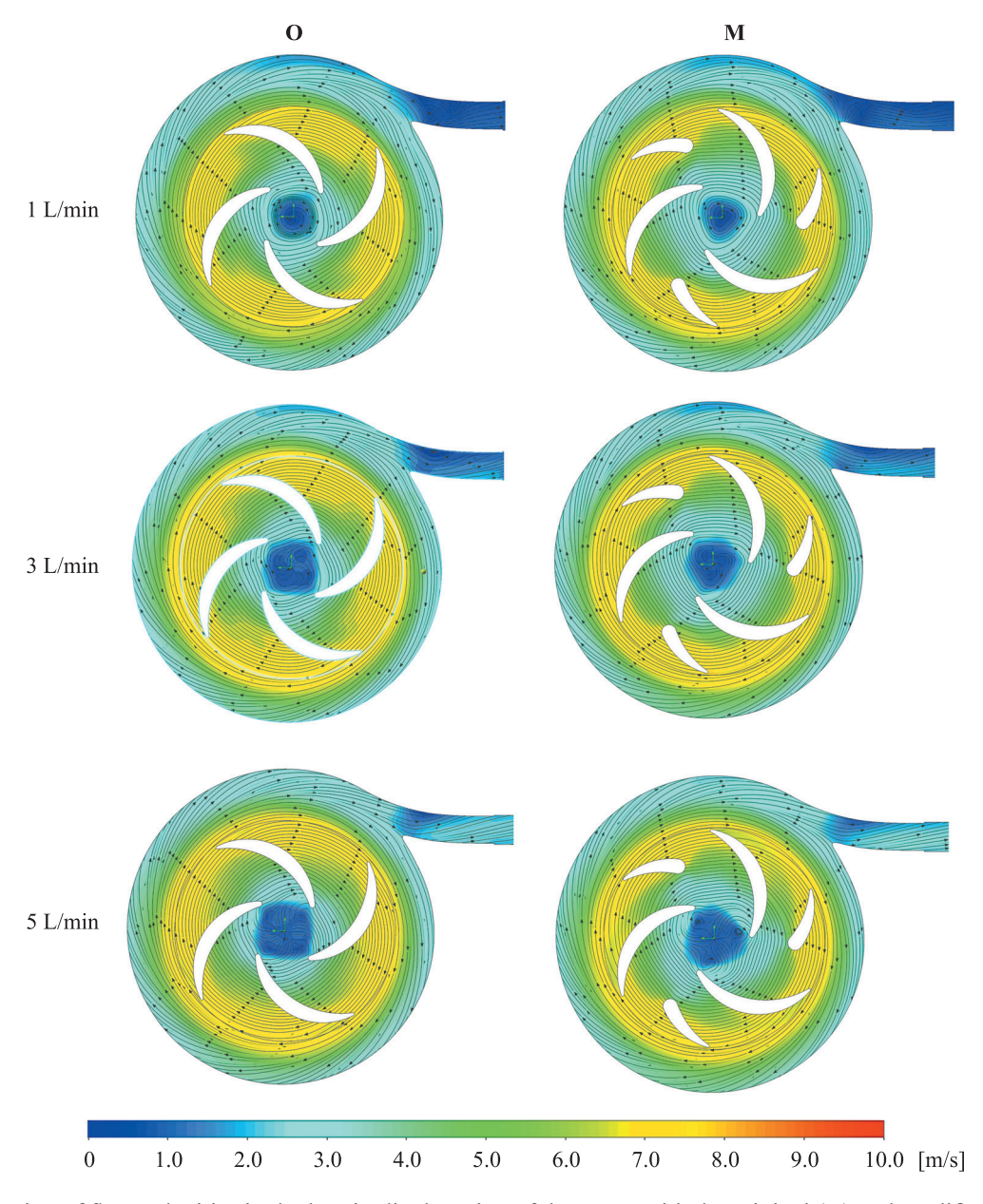


Fig. 6. Distribution of flow velocities in the longitudinal section of the pump with the original (O) and modified (M) impeller designs. Zones of active turbulence and flow stagnation are highlighted

Flow visualization showed a reduction in turbulence scale, with vortex size decreasing in the optimized model. At the same time, the average flow velocity and the number of visible vortices were moderately reduced. Collectively, these changes may contribute to a slight reduction in the overall mechanical load on blood cells.

A critical factor in optimizing centrifugal pump performance is maintaining smooth velocity transitions between surfaces in the flow region to minimize turbulence. This effect is evident in Figs. 5 and 6. While high Reynolds numbers were observed in both rotor models, the values were approximately 500 points lower in the modified design.

The distribution patterns of flow velocity vectors and turbulence parameters indicated turbulence at the rotor outlet and at the junction where channel flows entered the spiral volute. However, cross-sectional velocity vector plots showed a more balanced and uniform flow in the optimized rotor, contributing to reduced energy loss and lower shear stress.

Clear differences also emerged in the recirculation patterns at different flow rates. In both rotor models, decreasing flow rate led to the formation of recirculation zones at the junction of the spiral volute and the outlet tract, associated with a sharp edge commonly referred to as the "tongue". Notably, this recirculation zone was significantly larger in the original model, resulting in increased exposure time.

At higher rotational speeds and reduced flow rates, mutually oriented vortices, identified as Taylor–Couette vortices, were observed in both designs within the upper and lower gaps between the rotor and the housing (Fig. 7).

Analysis revealed that vortices at the blade tips were more pronounced in the original rotor compared to the modified design. This effect is attributed to the lower flow velocity and higher impeller rotation speed.

At low flow rates, the maximum number of particle trajectories with prolonged exposure times was observed. Under these conditions, particles tended to remain longer in the pump volute, with up to 30% of total trajectories

Table 1
Flow parameters of the pump with the original and modified impeller designs

Flow parameters	(Pressure 350 mm Hg, flow rate 1 L/min)		(Pressure 350 mm Hg, flow rate 3 L/min)		(Pressure 350 mm Hg, flow rate 5 L/min)	
Model	Original	Modified	Original	Modified	Original	Modified
Impeller rotation speed, rpm	3470	3375	3535	3445	3595	3505
Turbulence scale, mm (avg./max.)	0.37 / 0.70	0.44 / 0.68	0.33 / 0.62	0.26 / 1.03	0.71 / 1.02	0.71 / 1.2
Turbulence intensity, %	40 / 211	20 / 118	18 / 247	30 / 223	13 / 474	15 / 823
Exposure time, sec (avg./max.)	0.53 / 0.87	0.32 / 0.51	0.28 / 0.438	0.3 / 0.45	0.27 / 0.34	0.31 / 0.41
Maximum speed, m/s	3.5 / 9.0	3.4 / 8.9	3.6 / 9.3	3.6 / 9.0	3.4 / 9.2	3.5 / 9.1
Reynolds number	25505	25034	26026	25322	26243	25531

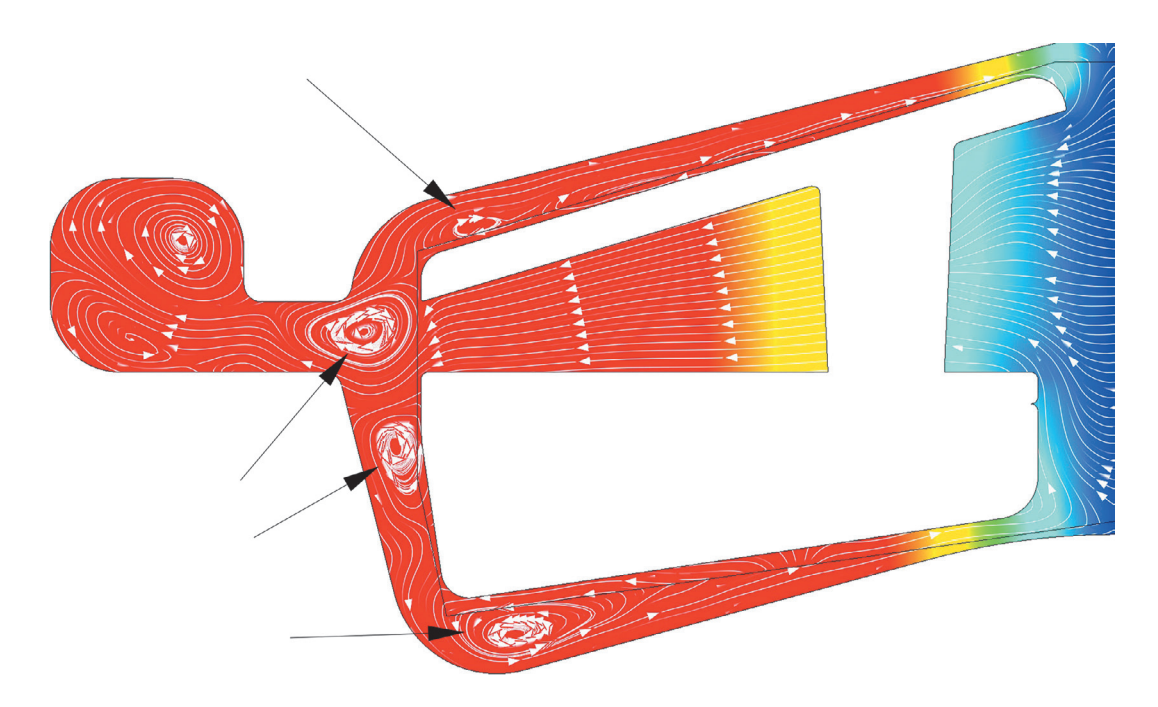


Fig. 7. Formation of Taylor-Couette vortices in the flow path of the pump at a flow rate of 1 L/min

entering recirculation zones. The presence of Taylor—Couette vortices substantially increased the residence time of particles, as these vortical structures promoted reverse flow and swirling motion. This reverse swirling was especially evident in the inlet pipe near the wall (Fig. 7).

To validate these findings, additional simulations were performed using both water and Newtonian blood models. The reverse flow phenomenon was consistently observed at 1 L/min and persisted at 3 L/min. However, at 5 L/min, the phenomenon was absent.

Pump efficiency is a key economic and technological parameter. Modern standards require that centrifugal pumps achieve a minimum efficiency of at least 65% at nominal load to ensure energy-efficient operation. In ECMO systems, however, this indicator decreases sharply due to the necessity of miniaturization.

According to an empirical rule, pump efficiency is strongly dependent on impeller size. For geometrically similar pumps, doubling the impeller diameter increases efficiency by 5–8 percentage points [5]. This is due to changes in the surface-area-to-volume ratio and the resulting reduction in relative hydraulic losses, and is explained by efficiency gain formula (3):

$$\Delta \eta \approx 6\% \cdot \log(D_1/D_2),$$
 (3)

where  $D_1$  and  $D_2$  are rotor diameters before and after modification. Similarly, an increase in pump flow rate contributes positively to efficiency, as shown by ratio (4):

$$\eta_{\text{max}} \approx 0.8 + 0.0323 \cdot \log(Q), \tag{4}$$

where Q is volumetric flow rate [m³/h]. An empirical rule for the practical application of affinity laws states that a 10% increase in speed results in an approx. 10% increase in flow and a 21% increase in pressure; a 10% decrease in speed reduces the flow by 10% and the pressure by 19% [5]. The modified rotor design leveraged these principles. Although the rotor speed was reduced, the improved impeller geometry preserved both flow rate and pressure head. Consequently, the rotor modifications resulted in a slight increase in overall system efficiency, as summarized in Table 2.

# **CONCLUSION**

The laws of affinity for centrifugal pumps are valid within approximately  $\pm 30\%$  of the nominal rotational speed, with an accuracy of about 5%. However, when designing pumps for ECMO applications, other factors become equally critical, particularly blood trauma and low priming volume, which are especially important in pediatric use.

To address these requirements, the flow path must incorporate smooth geometric transitions and a highly efficient impeller that operates effectively at minimum speeds and relatively low flow rates. These conditions, however, make it inherently difficult to achieve the high

Table 2
Comparison of pump efficiency using the original and modified rotor designs

	Efficiency, %		
Rotor	Original	Modified	
Flow rate 1 L/min	47.7	48.3	
Flow rate 3 L/min	39.7	40.2	
Flow rate 5 L/min	14.0	15.2	

efficiencies typically expected of centrifugal systems. Furthermore, it is not practical to operate pumps across their entire HCC range, since large deviations from the design operating point inevitably result in loss of hydraulic efficiency and unstable flow regimes.

The results of this study demonstrate that transitioning to a rotor design with three long and three short blades offers clear advantages, including improved hydrodynamics and reduced shear stress. Nonetheless, the development of a line of pumps that can cover the flow and pressure range for different patient populations remains essential.

The authors declare no conflict of interest.

#### **REFERENCES**

- 1. *Gautier SV, Poptsov VN, Spirina EA*. Ekstrakorporal'naya membrannaya oksigenatsii kardiokhirurgii i transplantologii. M.: Triada, 2013; 272.
- 2. *Orime Y, Shiono M, Yagi S.* Jostra Rota Flow RF-30 Pump System: A New Centrifugal Blood Pump for Cardiopulmonary BypassCEntrimag. *Artificial Organs*. 2000; 24 (6): 437–441.
- Nagaoka E et al. MedTech Mag-Lev, single-use, extracorporeal magnetically levitated centrifugal blood pump for mid-term circulatory support. ASAIO J. 2013. 59: 246–252.
- 4. Fleck T, Benk C, Klemm R et al. First serial in vivo results of mechanical circulatory support in children with a new diagonal pump. Eur J Cardiothorac Surg. 2013; 44 (5): 828–835. doi: 10.1093/ejcts/ezt427.
- 5. *Karelin VYa, Minaev AV.* Nasosy i nasosnye stantsii. M.: Stroyizdat, 2016; 320.
- Liu GM, Jin DH, Jiang XH et al. Numerical and In Vitro Experimental Investigation of the Hemolytic Performance at the Off-Design Point of an Axial Ventricular Assist Pump. ASAIO J. 2016; 62 (6): 657–665. doi: 10.1097/MAT.00000000000000429.
- 7. Hastings SM, Ku DN, Wagoner S et al. Sources of circuit thrombosis in pediatric extracorporeal membrane oxygenation. ASAIO J. 2017. 63: 86–92.
- Buchnev AS, Kuleshov AP, Esipova OYu, Drobyshev AA, Grudinin NV. Hemodynamic evaluation of pulsatile-flow generating device in left ventricular assist devices. Russian Journal of Transplantology and Artificial Organs. 2023; 25 (1): 106–112. https://doi.org/10.15825/1995-1191-2023-1-106-112.

- 9. *Itkin GP, Bychnev AS, Kuleshov AP et al.* Haemodynamic evaluation of the new pulsatile-flow generation method *in vitro. The International Journal of Artificial Organs.* 2020; 43 (6): 157–164.
- 10. Roberts N, Chandrasekaran U, Das S et al. Hemolysis associated with Impella heart pump positioning: In vitro hemolysis testing and computational fluid dynamics modeling. Int J Artif Organs. 2020. Mar 4: 391398820909843. doi: 10.1177/0391398820909843.
- 11. *Li P, Mei X, Ge W et al.* A comprehensive comparison of the *in vitro* hemocompatibility of extracorporeal centrifugal blood pumps. *Front Physiol.* 2023. May 9; 14: 1136545. doi: 10.3389/fphys.2023.1136545.

- 12. Kilic A, Nolan TD, Li T et al. Early in vivo experience with the pediatric Jarvik 2000 heart. ASAIO J. 2007; 53 (3): 374–378. doi: 10.1097/MAT.0b013e318038fc1f.
- 13. *Tanikawa C, Kamatani Y, Terao C et al.* Risk Loci Identified in a Genome-Wide Association Study of Urolithiasis in a Japanese Population. *J Am Soc Nephrol.* 2019; 30 (5): 855–864. doi: 10.1681/ASN.2018090942.
- Fiusco F, Broman LM, Prahl Wittberg L. Blood Pumps for Extracorporeal Membrane Oxygenation: Platelet Activation During Different Operating Conditions. ASAIO J. 2022; 68 (1): 79–86. doi: 10.1097/ MAT.00000000000001493.

The article was submitted to the journal on 5.06.2025